Incremental viscoelasticity at finite strains for the modelling of 3D concrete printing

Boumediene Nedjar

Computational Mechanics manuscript No.
(will be inserted by the editor)

Incremental viscoelasticity at finite strains for the modelling of 3D concrete printing

B. Nedjar

Received: date / Accepted: date

Abstract Within a 3D concrete printing process, the fresh concrete is aging due to hydration. One of the consequences from the purely mechanical point of view is that its constitutive relation must be defined in rate form. This restriction is taken into account in this contribution and, besides on the incremental elasticity, we moreover introduce the relaxation of the internal stresses in order to describe the creep at early age. On another hand, due to the soft nature of the material, the finite strain range is herein a priori assumed. Eventual structural instabilities during the printing process can therefore be predicted as well. On another hand, with regards to the incremental formulation of the boundary value problem, the kinematics must be adapted as well. We use for this the multiplicative decomposition of the actual deformation gradient into its known part at an earlier time and the relative deformation gradient with respect to the configuration at that time. Within a Lagrangian formulation, the incremental constitutive relations and evolution equations can then be ideally defined on the above mentioned intermediate configuration prior to be transported back to the reference configuration. In particular, the early age creep is here described through an internal variable approach the evolution of which is motivated by the generalized Maxwell model. In this work, this latter is adapted for incremental viscoelasticity. Model examples are proposed and the numerical efficiency of the proposed framework is illustrated through a set of representative simulations.

B. Nedjar
Université Gustave Eiffel, MAST/EMGCU,
5 Boulevard Descartes,
77454 Marne-la-Vallée cedex 2, France
Tel.: +33-1-81668416
E-mail: boumediene.nedjar@univ-eiffel.fr

Keywords Additive manufacturing · Large deformation · Incremental formulation · Early age creep · Incremental viscoelasticity at finite strains

1 Introduction

Nowadays, the challenging 3D concrete printing is receiving considerable attention in the civil engineering industry; the 'Construction 4.0' as termed in [3]. In general, a concrete mixing is pumped into a pipe connected to a nozzle, and with the help of a robotic mechanism, precise positioning control and deposition path can be achieved. Potential applications of this promising new production process include, for instance, connection elements, structural elements, up to complete buildings, see for example [10, 9, 25] to mention a few.

The 3D printing technology is mostly based on additive manufacturing, i.e. the extrusion technique consists on the successive addition of material layer-by-layer. After several layers have been deposited onto each other, the fresh concrete must be able to retain its shape. Its buildability is then largely influenced by its early age mechanical properties and rheology, e.g. see for example [17, 8, 12]. Mathematical models must then take into account these properties for efficient predictive simulations and numerical design. Recently, numerical models have been proposed in the literature; continuum methods [21, 22, 26], as well as the pioneering work in [26] with discrete methods. For the former, finite element analyses have been conducted with time-dependent linear elasticity in combination with time-dependent plastic failure criteria. The authors reported promising results that seem in close agreement with the experimental results. However, the particularity of an aging concrete is its maturation as a result of hydration, e.g. [4].

As was shown in [1], one of the consequences is that the only possible way to express the constitutive relation would be in incremental form and not in direct form, see also [5,2] among others. Unlike the modelling framework adopted in the above references, this restriction will be taken into account in this work as in [14].

With the lack of confining formwork, the fresh concrete must carry its self-weight, especially when layers are being deposited one-by-one. However, as the resistance is initially low, possible collapse during the printing process can occur, e.g. [20,23]. A predictive theory must therefore be established within a geometrically nonlinear framework to be able to predict such instabilities. From the purely mechanical point of view, an incremental formulation has recently been developed in [14] where the kinematical choice has been based on the *natural* multiplicative decomposition of the actual deformation gradient, say at time t, into its known part at an earlier time, say at time t_n, and the relative deformation gradient with respect to the configuration at that time, i.e. within the time interval $[t_n, t]$. Incremental elastic constitutive relations have been proposed that were inspired by nowadays classical models of the Saint-Venant and neoHooke types, e.g. see for instance [6,24,13]. These models are first ideally defined on the above *known* intermediate configuration prior to be pull-back to the reference (initial) configuration when a Lagrangian formulation is adopted for the boundary value problem.

The above framework is pursued in this contribution by furthermore taking into account creep at early age that is essential to predict the stress relaxation. Herein we postulate an incremental viscoelasticity modelling that is phenomenologically based on the concept of internal variables. It is analogous to a similar approach developed in the last decades within the finite strain range, e.g. see for example [6,7,19]. More precisely, suitable evolution equations are defined within the formalism of incremental constitutive relations, the whole motivated by the generalized Maxwell rheological model. The stress-like internal variables consist on overstresses that have the same structure as the thermodynamically equilibrated second Piola-Kirchhoff stress tensor increments. Even if the material properties of an aging concrete basically depend upon time-dependent hydration and temperature, herein focus is made on the purely mechanical aspects. The topic of thermo-hydric coupling will be addressed in a future contribution.

A further goal of this paper is the formulation of a numerical treatment to furnish computational tools for structural simulations which could help the optimization of the printing process, limiting then the number of costly physical experiments. The most relevant particularities of the proposed algorithmic design are highlighted for an easy implementation within the context of the finite element method. In addition to its conceptual simplicity, the numerical effort is of the order of that devoted for classical finite strain computations. Only a single local resolution procedure for the internal variable is appended at the integration points level, which renders the whole numerical procedure very efficient.

An outline of the paper is as follows. In Section 2, we recall the basic equations that are adapted for an incremental formulation together with the corresponding kinematical choices. The early age creep is then developed in Section 3 that is motivated by the generalized Maxwell rheological model and that is adapted to this framework. Then, in Section 4, the most relevant details of an implementation within the finite element method are given. Next, and for illustrative purposes, two sets of numerical simulations are given in Section 5. Finally, conclusions with perspectives are drawn in Section 6.

1.1 Notations

Throughout the paper, bold face characters refer to second- and fourth-order tensorial quantities. The notation $(\boldsymbol{.})^T$ is used for the transpose operator, and the double dot symbol ':' is used for double tensor contraction, i.e. for any second-order tensors $\boldsymbol{A}$ and $\boldsymbol{B}$, $\boldsymbol{A} : \boldsymbol{B} \equiv \mathrm{tr}[\boldsymbol{A}\boldsymbol{B}^T] = A_{ij}B_{ij}$ where, unless specified, summation over repeated indices is always assumed. The notation $\otimes$ stands for the tensorial product, i.e. in components, one has $(\boldsymbol{A} \otimes \boldsymbol{B})_{ijkl} = A_{ij}B_{kl}$. Furthermore, the dot operator $\dot{(\boldsymbol{.})}$ always refers to the material time derivative of the quantity $(\boldsymbol{.})$.

2 Boundary value problem and kinematics

The formulation is a priori developed within the finite strain range because of the soft nature of the fresh printed concrete. In this section, we recall the balance equation that is adapted to the incremental form of the constitutive relations. We discuss then the kinematics that best matches this particularity. Model examples will be addressed next in Section 3, see [14] for further details.

2.1 Mechanical balance

When undeformed and unstressed, the body occupies the reference configuration $\mathcal{B}_0$ with boundary $\partial\mathcal{B}_0$. We identify a material particle by its position vector $\boldsymbol{X} \in$

$\mathcal{B}_0$ and we trace its motion by its current position in the spatial configuration $\mathcal{B}_t$ at time t as $\boldsymbol{x} = \boldsymbol{\varphi}_t(\boldsymbol{X}) \in \mathcal{B}_t$ where $\boldsymbol{\varphi}_t(\boldsymbol{.}) \equiv \boldsymbol{\varphi}(\boldsymbol{.}, t)$ denotes the deformation map at time t within a time interval $[0, T]$. The deformation gradient is defined as $\boldsymbol{F} \equiv \boldsymbol{F}_t = \nabla_{\boldsymbol{X}} \boldsymbol{\varphi}$, where $\nabla_{\boldsymbol{X}}(\boldsymbol{.})$ is the material gradient operator with respect to $\boldsymbol{X}$. The Jacobian of the transformation is given by the determinant $J = \det \boldsymbol{F}$ with the standard convention $J > 0$.

Within a Lagrangian formulation, the mechanical equilibrium with respect to the initial configuration is equivalently given by the following weak form in terms of the second Piola-Kirchhoff stress tensor $\boldsymbol{S} \equiv \boldsymbol{S}_t$:

$$\int_{\mathcal{B}_0} \boldsymbol{S} : \boldsymbol{F}^T \nabla_{\boldsymbol{X}}(\delta\boldsymbol{\varphi}) \, \mathrm{d}V = \int_{\mathcal{B}_0} \rho_0 \bar{\boldsymbol{b}}.\delta\boldsymbol{\varphi} \, \mathrm{d}V \ , \tag{1}$$

which must hold for any admissible variation of deformation $\delta\boldsymbol{\varphi}$. Here the vector $\rho_0\bar{\boldsymbol{b}}$ defines the body force due to gravitation, i.e. the self-weight, where ρ_0 is the initial density. Unlike classical constitutive relations where the stress is directly linked to strain measures, i.e. for instance as this would be the case for a hyperlastic material through a strain energy function, the stress tensor is restricted to be solely defined in incremental form in our case. Herein, within a typical time interval $[t_n, t_{n+1}]$, we make the following choice for the second Piola-Kirchhoff stress tensor:

$$\boldsymbol{S} = \boldsymbol{S}_n + \Delta\boldsymbol{S} \ , \tag{2}$$

where $\boldsymbol{S}_n$ is the *known* second-Piola Kirchhoff stress tensor at time t_n, and $\Delta\boldsymbol{S} \equiv \Delta\boldsymbol{S}_t$ is the second Piola-Kirchhoff stress tensor increment at the actual time $t \in [t_n, t_{n+1}]$. Thus, when replacing (2) into (1), we end up with the basic balance equation to be solved in our formulation:

$$\int_{\mathcal{B}_0} (\boldsymbol{S}_n + \Delta\boldsymbol{S}) : \boldsymbol{F}^T \nabla_{\boldsymbol{X}}(\delta\boldsymbol{\varphi}) \, \mathrm{d}V = \int_{\mathcal{B}_0} \rho_0 \bar{\boldsymbol{b}}.\delta\boldsymbol{\varphi} \, \mathrm{d}V \ . \tag{3}$$

This latter equation is valid for all classes of *incremental* constitutive relations through the definition of model-dependent stress increment $\Delta\boldsymbol{S}$ including, for instance, creep and/or plasticity. Notice that the deformation gradient $\boldsymbol{F}$ in (3) is the actual one $\boldsymbol{F}_t$ at time t. Furthermore, the gravitation force does not need to be incremented, which is crucial for the modelling of the 3D concrete printing process.

2.2 Linearization of the mechanical balance

The incremental form (3) is highly nonlinear. In the one hand because of the geometrical nonlinearities, and on the other hand because of nonlinearities stemming from the incremental constitutive relations. Its linearization is then necessary as the problem needs to be solved numerically by the use of an iterative solution strategy of Newton's type within the finite element method.

Denoting as customary by $\boldsymbol{u}(\boldsymbol{X})$ the displacement of a particle $\boldsymbol{X} \in \mathcal{B}_0$ such that $\boldsymbol{\varphi}(\boldsymbol{X}) = \boldsymbol{X} + \boldsymbol{u}(\boldsymbol{X})$, the linearization of Eq. (3) is computed at a deformation map $\overline{\boldsymbol{\varphi}} = \boldsymbol{\varphi}_n + \Delta\boldsymbol{u}$ where $\boldsymbol{\varphi}_n = \boldsymbol{X} + \boldsymbol{u}_n(\boldsymbol{X})$ is the known deformation at time t_n, and $\Delta\boldsymbol{u}$ is the iteratively updated displacement increment. Following standard procedures, e.g. for instance [18,6,24,15], one obtains,

$$\begin{aligned} \int_{\mathcal{B}_0} \Big\{ \nabla_{\boldsymbol{X}}(\Delta\boldsymbol{u}) \, (\boldsymbol{S}_n + \Delta\boldsymbol{S}) : \nabla_{\boldsymbol{X}}(\delta\boldsymbol{\varphi}) + \delta\boldsymbol{E} : \overline{\boldsymbol{\Xi}}^{\mathrm{algo}} : \Delta\boldsymbol{E} \Big\} \, \mathrm{d}V \\ = \int_{\mathcal{B}_0} \Big\{ \rho_0 \bar{\boldsymbol{b}}.\delta\boldsymbol{\varphi} - (\boldsymbol{S}_n + \Delta\boldsymbol{S}) : \delta\boldsymbol{E} \Big\} \, \mathrm{d}V \ , \end{aligned} \tag{4}$$

where $\delta\boldsymbol{E}$ and $\Delta\boldsymbol{E}$ are respectively the variation and the linearization of the Green-Lagrange strain tensor[1] given by,

$$\begin{aligned} \delta\boldsymbol{E} &= \frac{1}{2}\Big\{ \boldsymbol{F}^T \nabla_{\boldsymbol{X}}(\delta\boldsymbol{\varphi}) + \nabla_{\boldsymbol{X}}^T(\delta\boldsymbol{\varphi}) \boldsymbol{F} \Big\} \ , \\ \Delta\boldsymbol{E} &= \frac{1}{2}\Big\{ \boldsymbol{F}^T \nabla_{\boldsymbol{X}}(\Delta\boldsymbol{u}) + \nabla_{\boldsymbol{X}}^T(\Delta\boldsymbol{u}) \boldsymbol{F} \Big\} \ , \end{aligned} \tag{5}$$

and where $\overline{\boldsymbol{\Xi}}^{\mathrm{algo}}$ is the fourth-order (algorithmic) tangent modulus that depends on the incremental constitutive relation, see below in Section 3. The first term in the left hand-side of Eq. (4) is the so-called geometrical part and the second term is the material part. The right-hand of (4) is the residual. Notice that the stress tensor increment $\Delta\boldsymbol{S}$ and the tangent modulus $\overline{\boldsymbol{\Xi}}^{\mathrm{algo}}$ have to be evaluated at $\overline{\boldsymbol{\varphi}}$. Equation (4) is to be solved together with the local evolution equation appended: the over-stress evolution due to the incremental viscoelasticity, see below as well.

2.3 Kinematic assumption and structure of the incremental constitutive relations

The kinematical choice must be adapted for a sound definition of an incremental constitutive relation. We choose for this the nowadays well-known multiplicative decomposition of the deformation gradient into its known part at an earlier time and the relative deformation gradient, e.g. [19,18,14] among others. Let $\boldsymbol{F}_n$ be

[1] We recall the definition of the Green-Lagrange strain tensor: $\boldsymbol{E} = \frac{1}{2}\{\boldsymbol{C} - \boldsymbol{1}\}$, where $\boldsymbol{C} = \boldsymbol{F}^T\boldsymbol{F}$ is the right Cauchy-Green tensor and $\boldsymbol{1}$ is the second-order identity tensor.

the deformation gradient at time t_n, the actual deformation gradient $\boldsymbol{F}$ at time $t \in [t_n, t_{n+1}]$ is given by,

$$\boldsymbol{F} = \tilde{\boldsymbol{f}}\boldsymbol{F}_n \ , \tag{6}$$

where $\tilde{\boldsymbol{f}} \equiv \tilde{\boldsymbol{f}}_t$ is the relative deformation gradient, see the sketch of Fig. 1 for an illustration. With this latter one can define the relative right Cauchy-Green tensor $\tilde{\boldsymbol{c}}$ with respect to the intermediate configuration $\boldsymbol{\varphi}_n$ as,

$$\tilde{\boldsymbol{c}} = \tilde{\boldsymbol{f}}^T\tilde{\boldsymbol{f}} \ . \tag{7}$$

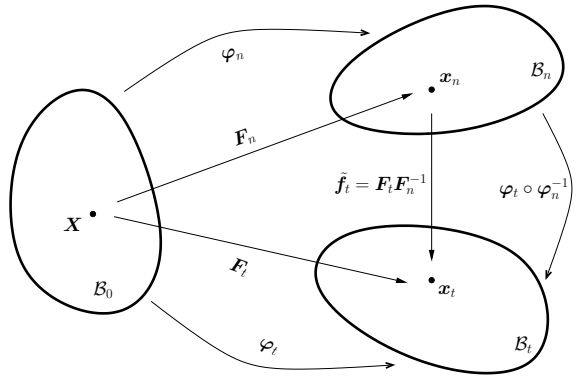

Fig. 1 Relative deformation gradient $\tilde{\boldsymbol{f}}_t$ connecting configurations $\mathcal{B}_n$ and $\mathcal{B}_t$. $\boldsymbol{F}_n$ is the total deformation gradient at time t_n, and $\boldsymbol{F}_t$ is its update at time $t \in [t_n, t_{n+1}]$.

For later use, one has moreover the following useful kinematical relation connecting $\tilde{\boldsymbol{c}}$ with the (total) right Cauchy-Green tensor $\boldsymbol{C} = \boldsymbol{F}^T\boldsymbol{F}$:

$$\tilde{\boldsymbol{c}} = \boldsymbol{F}_n^{-T}\boldsymbol{C}\boldsymbol{F}_n^{-1} \ . \tag{8}$$

Formally, the incremental stress is first defined on the intermediate configuration $\boldsymbol{\varphi}_n$ where one can define the second Piola-Kirchhoff-type stress tensor increment that we denote by $\tilde{\boldsymbol{s}}$ with the form,

$$\tilde{\boldsymbol{s}} \equiv \tilde{\boldsymbol{s}}(\tilde{\boldsymbol{c}}, \dots) \ , \tag{9}$$

in terms of the relative right Cauchy-Green tensor, and the dots refering to eventual internal variable. This stress increment is then transformed back to the reference configuration with the help of the appropriate tensorial procedure,

$$\boldsymbol{\Delta S} = \boldsymbol{F}_n^{-1}\,\tilde{\boldsymbol{s}}\,\boldsymbol{F}_n^{-T} \ . \tag{10}$$

The result of Eq. (10) is to be replaced in the balance equation (3), and hence in the linearized form (4). In a geometric context, we refer to (10) as a pull-back, e.g. [11]. The procedure (9)-(10) is well adapted for incremental models inspired by many classical hyperelastic ones, for instance, neoHooke, Mooney-Rivlin, classical Hencky, exponentiated Henchy, or even Ogden like models, e.g. [6,24,16,15] to mention a few.

3 Incremental viscoelastic constitutive relation

In this section we give a modeling example motivated by the generalized Maxwell rheological model, see Fig. 2. The second Piola-Kirchhoff stress $\boldsymbol{S}$ is additively split as,

$$\boldsymbol{S} = \boldsymbol{S}^{\infty} + \boldsymbol{Q} \ , \tag{11}$$

where $\boldsymbol{S}^{\infty}$ is the equilibrium part, and the introduced internal tensor variable $\boldsymbol{Q}$ may be interpreted as a non-equilibrium over-stress, e.g. [7,6,19]. Hence, within the time interval $[t_n, t_{n+1}]$, Eq. (2) becomes,

$$\boldsymbol{S} = \underbrace{\boldsymbol{S}_n^{\infty} + \boldsymbol{Q}_n}_{=\boldsymbol{S}_n} + \underbrace{\boldsymbol{\Delta S}^{\infty} + \boldsymbol{\Delta Q}}_{=\boldsymbol{\Delta S}} \ . \tag{12}$$

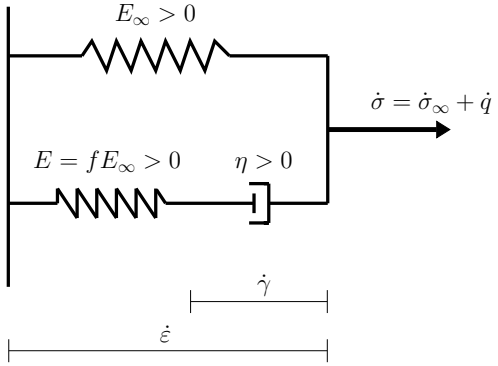

Fig. 2 Motivation: generalized Maxwell model.

In the following, we first define an incremental constitutive relation for the equilibrium part $\boldsymbol{\Delta S}^{\infty}$, and hence the update of $\boldsymbol{S}_{\infty}$. Then we define a local evolution equation for the internal variable $\boldsymbol{Q}$, and hence the over-stress increment $\boldsymbol{\Delta Q}$.

3.1 A model example for the equilibrium part

Within the finite srain range, many model examples can be proposed. In this contribution, we choose perhaps one of the most popular model in its hyperelastic version. Indeed, let us stress that one cannot invoque a strain energy function because of the *hypoelastic* character of the constitutive relation, i.e. given here in incremental form. Hence, inspired by a compressible version of the neoHooke model, we postulate the following relation for the equilibrated second Piola-Kirchhoff-type stress tensor increment $\tilde{\boldsymbol{s}}^{\infty}$ with respect to the configuration $\boldsymbol{\varphi}_n$, and in terms of the relative right Cauchy-

Green tensor[2]:

$$\tilde{\boldsymbol{s}}^{\infty} \;=\; \lambda_{\infty}(t)\,\log[\tilde{j}]\,\tilde{\boldsymbol{c}}^{-1} \;+\; \mu_{\infty}(t)\left(\mathbf{1}-\tilde{\boldsymbol{c}}^{-1}\right)\,, \tag{13}$$

where $\log[\boldsymbol{.}]$ is the natural logarithm function and $\tilde{j}$ is the jacobian of the relative deformation gradient:

$$\tilde{j} = \det[\tilde{\boldsymbol{f}}]\;. \tag{14}$$

Here and in all what follows, $\mathbf{1}$ is the second-order identity tensor with components δ_{ij} (δ_{ij} being the Kronecker delta). The time-dependent parameters $\lambda_{\infty}(t)$ and $\mu_{\infty}(t)$ are Lamé-like coefficients within the asymptotic infinitesimal limit. They are related to the time-dependent Young's modulus $E_{\infty}(t)$ and Poisson's ratio $\nu(t)$ of the equilibrium part as:

$$\begin{aligned}\lambda_{\infty}(t) &= \frac{\nu(t)\,E_{\infty}(t)}{(1+\nu(t))(1-2\nu(t))}\;,\\ \mu_{\infty}(t) &= \frac{E_{\infty}(t)}{2(1+\nu(t))}\;.\end{aligned} \tag{15}$$

Then, the pull-back relation (10) applied to (13) gives the following expression for the equilibrium second Piola-Kirchhoff stress increment:

$$\Delta\boldsymbol{S}^{\infty} = \lambda_{\infty}(t)\,\log\left[\frac{J}{J_n}\right]\boldsymbol{C}^{-1} + \mu_{\infty}(t)\Big(\boldsymbol{C}_n^{-1}-\boldsymbol{C}^{-1}\Big), \tag{16}$$

where $J_n = \det\boldsymbol{F}_n$, $\boldsymbol{C}_n = \boldsymbol{F}_n^T\boldsymbol{F}_n$, and use has been made of the kinematic relation $J = \tilde{j}J_n$.

Useful for the linearized form (4), the fourth-order tangent modulus relative to the equilibrium part is obtained by the derivation with respect to the right Cauchy-Green tensor as,

$$\begin{aligned}\overline{\boldsymbol{\Xi}}^{\infty} &= \frac{\partial\Delta\boldsymbol{S}^{\infty}}{\partial\boldsymbol{E}} \equiv 2\,\frac{\partial\Delta\boldsymbol{S}^{\infty}}{\partial\boldsymbol{C}}\\ &= \lambda_{\infty}(t)\;\boldsymbol{C}^{-1}\otimes\boldsymbol{C}^{-1}\\ &\quad + 2\Big(\mu_{\infty}(t)-\lambda_{\infty}(t)\,\log\left[\frac{J}{J_n}\right]\Big)\;\boldsymbol{I}_{\boldsymbol{C}^{-1}}\;,\end{aligned} \tag{17}$$

where the fourth-order tensor $\boldsymbol{I}_{\boldsymbol{C}^{-1}}$ is such that $\boldsymbol{I}_{\boldsymbol{C}^{-1}} : \boldsymbol{A} = \boldsymbol{C}^{-1}\boldsymbol{A}\boldsymbol{C}^{-1}$ for any second-order tensor $\boldsymbol{A}$, in components, e.g. [6,19,24]:

$$I_{ABCD} = \frac{1}{2}\Big\{C^{-1}_{AC}\,C^{-1}_{BD} \;+\; C^{-1}_{AD}\,C^{-1}_{BC}\Big\}\;. \tag{18}$$

[2] For the hyperelastic version of the model of Eq. (13), the strain energy function would be $W^{\infty} = \frac{1}{2}\lambda_{\infty}\log^2[J] - \mu_{\infty}\log[J] + \frac{1}{2}\mu_{\infty}(\boldsymbol{C} : \mathbf{1} - 3)$ in terms of the (total) right Cauchy-Green tensor $\boldsymbol{C}$. With the state law $\boldsymbol{S}_{\infty} = \frac{\partial W^{\infty}}{\partial\boldsymbol{C}}$, this gives $\boldsymbol{S}_{\infty} = \lambda_{\infty}\log[J]\boldsymbol{C}^{-1} + \mu_{\infty}(\mathbf{1}-\boldsymbol{C}^{-1})$.

3.2 Evolution equation for the internal variable

To describe the incremental viscoelasticity, it is necessary to specify a complementary equation of evolution that governs the internal variable $\boldsymbol{Q}$. At first, this is motivated by the following geometrically linear one-dimensional analyzis.

3.2.1 Motivation. One-dimensional linear geometry

The model of Fig. 2 consists of a spring with constant $E_{\infty} \equiv E_{\infty}(t)$ representing the equilibrium part, in parallel with a Maxwell element. This latter consisting of a dashpot with contant $\eta(t)$ in series with a spring of constant $E(t) = fE_{\infty}(t)$, where f is an adimensional factor chosen here to be *constant*. The incremental relations in each element are given by,

$$\begin{aligned}&\dot{\sigma}_{\infty} = E_{\infty}\,\dot{\varepsilon}\;,\\ &q = \eta\,\dot{\gamma} \quad\Rightarrow\quad \dot{q} = \eta\,\ddot{\gamma} + \dot{\eta}\,\dot{\gamma}\;,\end{aligned} \tag{19}$$

where $\dot{\varepsilon}$ and $\dot{\gamma}$ are respectively the total and viscous strain rates, i.e. strain increment quantities. Analyzing the Maxwell element, the incremental stresses in the dasphot and the spring are equal:

$$\eta\,\ddot{\gamma} + \dot{\eta}\,\dot{\gamma} \;=\; fE_{\infty}(\dot{\varepsilon}-\dot{\gamma})\;. \tag{20}$$

Let us now define the characteristic time τ of the dashpot as:

$$\tau \;=\; \frac{\eta}{fE_{\infty}} \;=\; \frac{\dot{\eta}}{f\dot{E}_{\infty}}\;. \tag{21}$$

Replacing this latter into (20), one obtains the following important second-order evolution equation for the strain-like internal variable γ,

$$\ddot{\gamma} \;+\; \underbrace{\Big(\frac{\dot{E}_{\infty}}{E_{\infty}}+\frac{1}{\tau}\Big)}_{=\,\omega}\dot{\gamma} \;=\; \frac{1}{\tau}\,\dot{\varepsilon}\;. \tag{22}$$

Within a time interval $[t_n, t_{n+1}]$, an exponential approximation to Eq. (22) can be used to solve for $\dot{\gamma}_{n+1}$ at time t_{n+1}. This leads to the following first-order accurate equation:

$$\dot{\gamma}_{n+1} \;=\; \frac{1-e^{-\omega\Delta t}}{\omega\tau}\,\dot{\varepsilon} \;+\; e^{-\omega\Delta t}\,\dot{\gamma}_n\;, \tag{23}$$

where $\Delta t = t_{n+1}-t_n$, $\dot{\gamma}_n$ is the initial solution at time t_n, and where ω is supposed to be constant within the time interval $[t_n, t_{n+1}]$.

To go further, instead of solving for the strain-like rate of internal variable, it is best suited to solve for

the stress-like internal variable q. Hence, by using the relation $(19)_2$, i.e. $q = \eta\,\dot\gamma$, we end up with the following internal over-stress update equation:

$$q_{n+1} \;=\; e^{-\omega\Delta t}\,q_n \;+\; \big(1-e^{-\omega\Delta t}\big)\,\frac{f}{\omega\Delta t}\,\underbrace{E_\infty\Delta\varepsilon}_{=\,\Delta\sigma_\infty}\;, \tag{24}$$

where $q_n \equiv \eta\,\dot\gamma_n$ is the initial solution at time t_n, and use has been made of the relation $(21)_1$ together with the approximation $\dot\varepsilon \approx \Delta\varepsilon/\Delta t$.

3.2.2 Evolution equation in the finite strain range

By reference to (24), we motivate the evolution equation for the three-dimensional and nonlinear deformation. Having this in mind, an obvious choice of appropriate evolution equation for the internal stress-like internal variable $\boldsymbol{Q}$ within the time interval $[t_n, t_{n+1}]$ has the form,

$$\boldsymbol{Q}_{n+1} \;=\; e^{-\omega\Delta t}\,\boldsymbol{Q}_n \;+\; f\,\frac{1-e^{-\omega\Delta t}}{\omega\Delta t}\,\Delta\boldsymbol{S}^\infty\;, \tag{25}$$

where $\boldsymbol{Q}_n$ is the known (stored) value of $\boldsymbol{Q}$ at time t_n, and ΔS^∞ is the equilibrium second Piola-Kirchhoff stress increment that has been evaluated by Eq. (16). The quantity ω is given by,

$$\omega \;=\; \frac{\dot E_\infty}{E_\infty} + \frac{1}{\tau}\;. \tag{26}$$

and is considered as constant within the time interval.

Once $\boldsymbol{Q}_{n+1}$ is updated with the help of Eq. (25), the difference $\Delta\boldsymbol{Q} = \boldsymbol{Q}_{n+1} - \boldsymbol{Q}_n$ is to be evaluated and replaced into Eq. (12) for the stress increment $\Delta\boldsymbol{S}$.

Useful for the linearization (4), the fourth-order tangent modulus relative to the non-equilibrium part is simply given by,

$$\overline{\boldsymbol{\Xi}}^{\rm neq} \equiv \frac{\partial\Delta\boldsymbol{Q}}{\partial\boldsymbol{E}} \;=\; f\,\frac{1-e^{-\omega\Delta t}}{\omega\Delta t}\,\overline{\boldsymbol{\Xi}}^{\infty}\;, \tag{27}$$

where $\overline{\boldsymbol{\Xi}}^{\infty}$ is the tangent modulus of the equilibrium part, Eq. (17). Hence, the algorithmic tangent modulus that is used in the linearized form (4) is simply given by,

$$\overline{\boldsymbol{\Xi}}^{\rm algo} = \Big(1 \,+\, f\,\frac{1-e^{-\omega\Delta t}}{\omega\Delta t}\Big)\,\overline{\boldsymbol{\Xi}}^{\infty}\;. \tag{28}$$

4 Finite element outlines

In a finite element context, the interpolations of the reference geometry and displacements are completely standard, see e.g. [24] for the exposition of these ideas. Over a typical finite element $\mathcal{B}_e$ they take the form,

$$\begin{aligned}\boldsymbol{X}_e(\boldsymbol{\zeta}) \;&=\; \sum_{A=1}^{n^e_{\rm node}} N^A(\boldsymbol{\zeta})\boldsymbol{X}^e_A\;,\\ \boldsymbol{u}_e(\boldsymbol{\zeta}) \;&=\; \sum_{A=1}^{n^e_{\rm node}} N^A(\boldsymbol{\zeta})\boldsymbol{u}^e_A\;,\end{aligned} \tag{29}$$

where $\boldsymbol{X}_A \in \mathbb{R}^{n_{\rm dim}}$, $\boldsymbol{u}_A \in \mathbb{R}^{n_{\rm dim}}$ denote the reference position and the displacement vector associated with the element node A, $n_{\rm dim} = 2$ or 3 is the space dimension, $n^e_{\rm node}$ is the node number within the element, and $N^A(\boldsymbol{\zeta})$ are the classical isoparametric shape functions. The interpolation of the deformation gradient then takes the form,

$$\begin{aligned}\boldsymbol{F}_e(\boldsymbol{\zeta}) \;&=\; \sum_{A=1}^{n^e_{\rm node}} (\boldsymbol{X}^e_A + \boldsymbol{u}^e_A)\otimes\nabla_{\boldsymbol{X}}[N^A]\;,\\ &\text{with } \nabla_{\boldsymbol{X}}[N^A] = \boldsymbol{J}(\boldsymbol{\zeta})^{-T}\nabla_{\boldsymbol{\zeta}}[N^A]\;,\end{aligned} \tag{30}$$

where $\nabla_{\boldsymbol{\zeta}}[\centerdot]$ is the gradient relative to the isoparametric coordinates, and $\boldsymbol{J}(\boldsymbol{\zeta}) = \partial\boldsymbol{X}_e(\boldsymbol{\zeta})/\partial\boldsymbol{\zeta}$ denotes the Jacobian of the isoparametric map $\boldsymbol{\zeta} \to \boldsymbol{X}$.

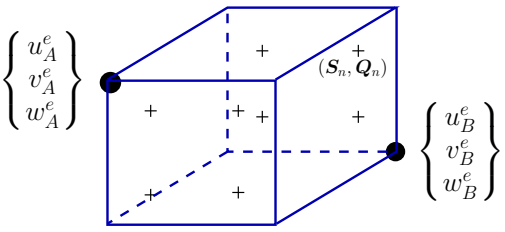

Fig. 3 Typical finite element with nodal *dof*s and integration points.

Equation $(30)_1$ is used for the discrete variation and increment of the Green-Lagrange strain tensor, Eq. (5), for instance for the latter:

$$\begin{aligned}\Delta\boldsymbol{E} &= \frac{1}{2}\sum_{A=1}^{n^e_{\rm node}}\Big[\boldsymbol{F}_e^T(\Delta\boldsymbol{u}^e_A\otimes\nabla_{\boldsymbol{X}}N^A) + (\nabla_{\boldsymbol{X}}N^A\otimes\Delta\boldsymbol{u}^e_A)\boldsymbol{F}_e\Big]\\ &= \sum_{A=1}^{n^e_{\rm node}}\mathbb{B}[N^A]\,\Delta\boldsymbol{u}^e_A\;,\end{aligned} \tag{31}$$

in terms of the nodal displacement increments $\Delta\boldsymbol{u}^e_A$, and where $\mathbb{B}[\centerdot]$ is the discrete Green-Lagrange strain

operator. The element contribution to the global tangent stiffness matrix and residual associated with the element nodes are written from (4) as,

$$\begin{aligned}\mathbf{K}_e^{AB} &= \int_{\mathcal{B}_e} \mathbb{B}^T[N^A]\,\overline{\boldsymbol{\Xi}}^{\text{algo}}\,\mathbb{B}[N^B]\,\mathrm{d}V_e \\ &\quad + \left\{\int_{\mathcal{B}_e} (\nabla_{\boldsymbol{X}}[N^A])^T(\boldsymbol{S}_n + \Delta\overline{\boldsymbol{S}})\,\nabla_{\boldsymbol{X}}[N^B]\,\mathrm{d}V_e\right\}\boldsymbol{I}_{n_{\text{dim}}}\ , \\ \mathbf{R}_e^A &= \int_{\mathcal{B}_e}\Big[N^A\rho_0\bar{\boldsymbol{b}} - \mathbb{B}^T[N^A]\,(\boldsymbol{S}_n + \Delta\overline{\boldsymbol{S}})\Big]\,\mathrm{d}V_e\ ,\end{aligned} \tag{32}$$

for $A, B = 1, \dots n^e_{\text{node}}$, see Fig. 3 for an illustration, and $\boldsymbol{I}_{n_{\text{dim}}}$ is the $n_{\text{dim}} \times n_{\text{dim}}$ identity matrix.

At the end of the global resolution, the stress field $\boldsymbol{S}_{n+1}$ and the updated stress-like internal variable $\boldsymbol{Q}_{n+1}$ via the evolution equation (25) are stored at the integration points level during the whole iterative process.

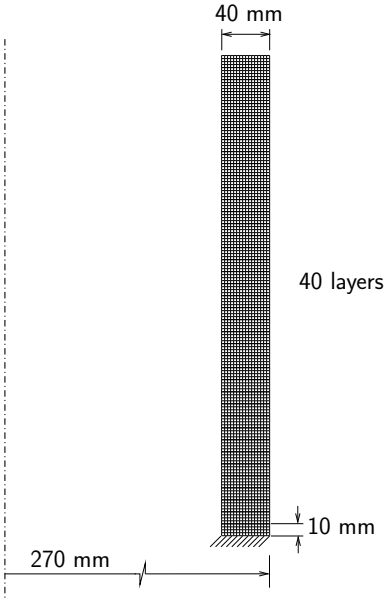

Fig. 4 Finite element mesh of a cylinder with 40 layers : a total of 2560 elements. The nodes of the bottom are fixed. The layers are activated one-by-one starting from the bottom during the printing process.

5 Numerical simulations

For illustrative purposes, we give in this section two sets of numerical simulations inspired by some examples found in the very recent litterature. The first one is for a printed cylinder held as a 2D-axisymmetric problem, and the second is a three-dimensional straight wall. Among others, we show that taking into account the early age creep can have a non negligeable influence on the final printed shapes.

5.1 A printed cylindrical geometry

We consider a cylindrical sample of external radius 270 mm, manufactured layer-by-layer, each layer with cross-sectional dimensions of 40 mm width and 10 mm height. The layers are added one-by-one at a speed of 0.31 minutes per layer until a maximum of 40 layers.

For the finite element simulations, each layer is discretized with axisymmetric 4-node quadrilateral elements with four elements through the layer thickness, and 16 elements along its width, i.e. a total of 64 elements per layer. Fig. 4 illustrates the initial mesh of the cylinder with 40 layers. Notice that only meridional buckling modes can be captured within this example.

For the fresh concrete, we choose the following time-dependent equilibrium Young's modulus and a constant Poisson ratio:

$$E_\infty(t) = 0.035 + 0.001\,t\ [\text{MPa}]\ , \qquad \nu = 0.3\ , \tag{33}$$

with the time t expressed in minutes. This modulus is calculated and updated for each layer during the analysis based on its age in the printing process. It enters into the definition of the Lamé-like coefficients given by Eq. (15). Finally, for the gravity loading the density is taken as

$$\rho_0 = 2070\,\text{kg/m}^3\ . \tag{34}$$

For the sake of comparison, a first simulation is conducted with no viscoelasticity activated in the model, i.e by taking $f = 0$. Fig. 5 shows selected deformed configurations with the radial displacement field u after 20 layers where the maximum obtained radial displacement is $u_{\max} = 9\,\text{mm}$, Fig. 5(a), after 28 layers where $u_{\max} = 19.2\,\text{mm}$, Fig. 5(b), and at the maximum reached by the computation after 31 layers where $u_{\max} = 33.64\,\text{mm}$, Fig. 5(c).

Further computations are now performed, this time with the activation of the incremental viscoelasticity. In addition to the parameters given by (33), two cases are considered here for the parameters f and τ:

$$\begin{aligned}&\textsf{case 1: } f = 0.5 \text{ and } \tau = 1\,\text{min}\ , \\ &\textsf{case 2: } f = 0.5 \text{ and } \tau = 10\,\text{min}\ ,\end{aligned} \tag{35}$$

that is, with the same over-stress levels but with different characteristic times.

For the first case, Fig. 6 shows the deformed configurations after 20, 30, and 40 layers. This time the com-

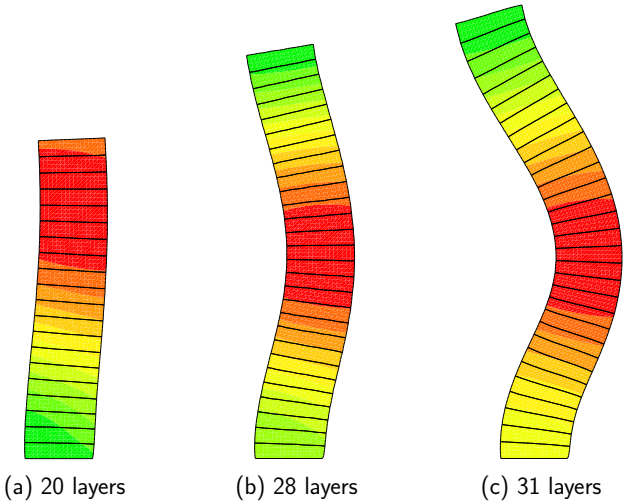

Fig. 5 Simulation with no viscoelasticity. Deformed configurations at scale 1 and radial displacement field u for the printed cylinder: (a) after 20 layers, (b) after 28 layers and, (c) at the maximum of 31 layers. The printing speed is 0.31 min per layer.

putation has reached all the modelled layers and, compared to the case without viscoelasticity, more structural stability is to be noticed due to the over-stresses. The maximum radial displacement is $u_{\max} = 6.25\,\text{mm}$ after 20 layers, 15.4 mm after 30 layers, and 62.35 mm after 40 layers.

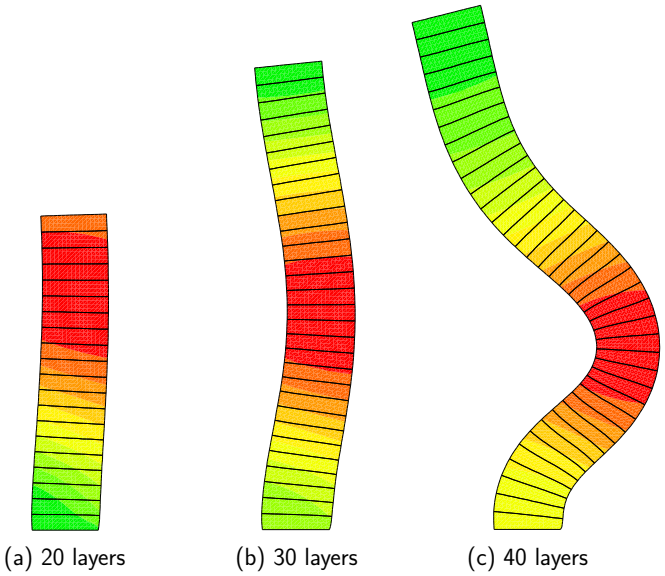

Fig. 6 Simulation with viscoelasticity, case 1: $f = 0.5$ and $\tau = 1\,\text{min}$. Deformed configurations and radial displacement field u for the printed cylinder after: (a) 20 layers, (b) 30 layers and, (c) 40 layers. The printing speed is 0.31 min per layer.

For the second case, Fig. 7 shows similarly the deformed configurations after 20, 30, and 40 layers. As expected, the displacements are this time of lower amplitudes than with the characteristic time $\tau = 1\,\text{min}$. Here the maximum radial displacement is $u_{\max} = 4.85\,\text{mm}$ after 20 layers, 10.6 mm after 30 layers, and 24 mm after 40 layers.

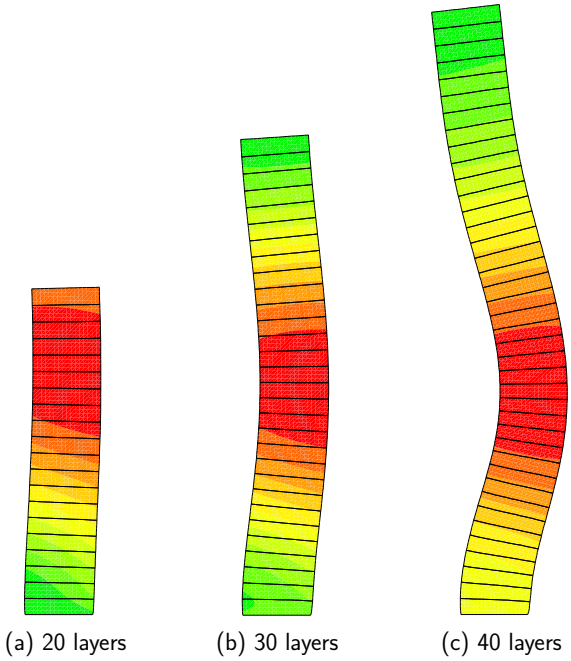

Fig. 7 Simulation with viscoelasticity, case 2: $f = 0.5$ and $\tau = 10\,\text{min}$. Deformed configurations and radial displacement field u for the printed cylinder after: (a) 20 layers, (b) 30 layers and, (c) 40 layers. The printing speed is 0.31 min per layer.

5.2 A 1 m printed concrete wall

We consider a 1 m straight wall manufactured layer-by-layer, each layer with cross-sectional dimensions of 60 mm width and 9.5 mm height. The layers are added step-by-step until divergence of the computational procedure due to structural buckling is observed. To trigger this latter, we a priori perform a geometrical imperfection by slightly tilting the cross-section of the wall: each layer is tilted 10^{-3} times the width of one layer, i.e. about 0.06 mm. This example has been studied in [14] under incremental elastic modelling.

For the finite element simulations, each layer is discretized with isoparametric 8-node hexahedral elements with two elements through the layer thickness, ten elements through its width, and 25 elements along the 1 m length, i.e. a total of 500 elements for each layer. Fig. 8 illustrates the initial mesh with 25 layers.

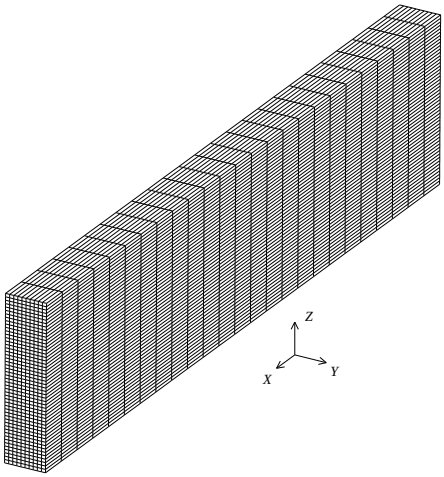

Fig. 8 Finite element mesh of a 1 m straight wall with 25 layers. The nodes of the bottom are fixed. The layers are activated one by one starting from the bottom during the printing process.

For the fresh concrete in the simulations below, we choose the following time-dependent equilibrium Young's modulus and constant Poisson ratio:

$$E_\infty(t) = 25.023 + 2.94\,t\ [\text{kPa}]\ , \qquad \nu = 0.3\ , \tag{36}$$

with $[t] = \text{min}$. Here again, this modulus is updated for each layer based on its age in the printing process. For the gravity loading, the density is taken as

$$\rho_0 = 2020\,\text{kg/m}^3\ . \tag{37}$$

In addition to the parameters given by (36), two cases are considered here for remaining ones:

$$\begin{array}{l}\text{case 1: } f = 0.2 \text{ and } \tau = 10\,\text{min}\ , \\ \text{case 2: } f = 1 \text{ and } \tau = 10\,\text{min}\ ,\end{array} \tag{38}$$

that is, this time with the same characteristic times, but with different over-stress levels. A printing speed of 0.3 min per layer is adopted in both simulations.

As buckling is expected, let us make the following indicative assumption: we consider that buckling occurs when the maximum out of plane deformations exceeds half layer-width, i.e. that is when the displacement component v in the Y-direction (see Fig. 8) is such that $v_{\max} \geq 30\,\text{mm}$.

For the first case, the simulation shows that the almost buckling occurs at layer 19 where the maximum out-of-plane displacement is $v_{\max} = 28.74\,\text{mm}$, see Fig. 9(b). We show in Fig. 9(a) the deformed configuration just before buckling: after 18 layers, and where the maximum displacement is $v_{\max} = 7.15\,\text{mm}$. And for illustrative purposes, Fig. 9(c) shows the post-buckling configuration after 20 layers where $v_{\max} = 158\,\text{mm}$.

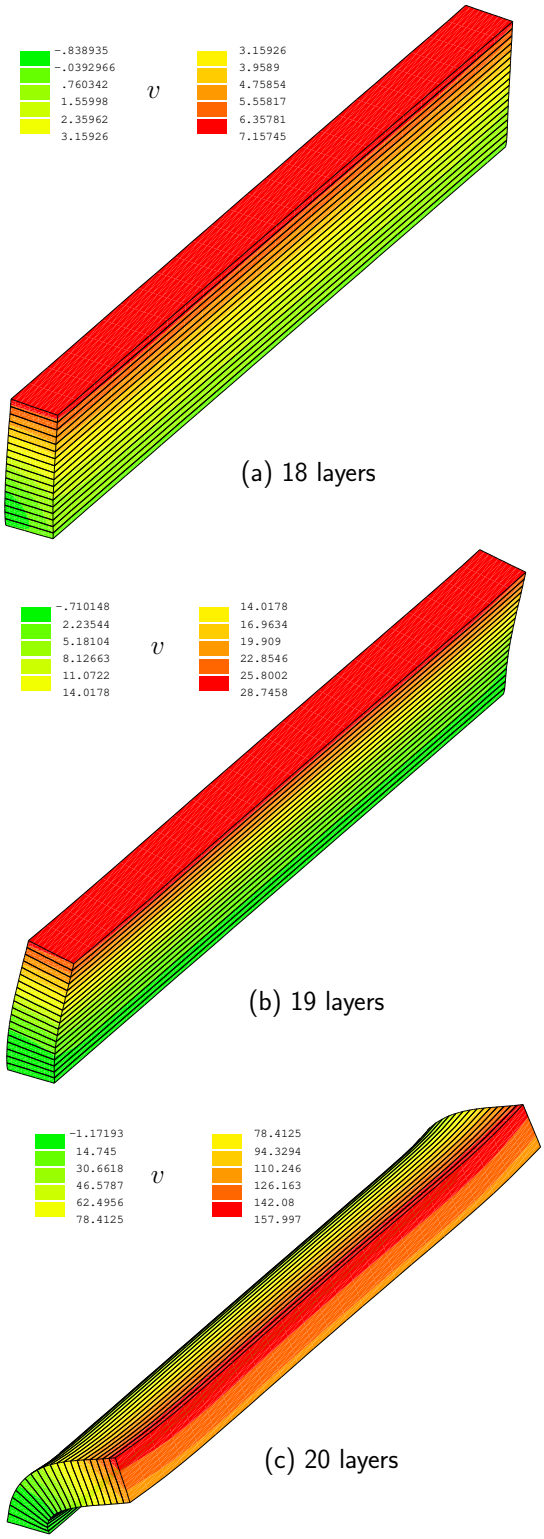

Fig. 9 Case 1 with $f = 0.2$ and $\tau = 10\,\text{min}$: deformed configurations and displacement field v for the 1 m wall after: (a) 18 layers, (b) 19 layers and, (c) 20 layers. Here the printing speed is 0.3 min per layer.

For case 2, Fig. 10(b) shows that this time buckling occurs after 23 layers with $v_{\max} = 46.8\,\text{mm}$. Here again, for illustrative purposes, Fig. 10(a) shows the deformed configurations after 22 layers just before buckling where $v_{\max} = 13.5\,\text{mm}$, and Fig. 10(c) after 25 layers where $v_{\max} = 222\,\text{mm}$, i.e. two layers after buckling criterion has been reached.

Last, the tentative curves shown in Fig. 11 summarize a comparative evolution of the maximum out-of-plane displacement with the number of printed layers.

6 Conclusions and perspectives

In this paper we have presented an extension to viscoelasticity of a recent theory for the modelling of the 3D concrete printing problem. Focusing on purely mechanical aspects, the fresh concrete has been described through time-dependent incremental constitutive relations in the finite strain range, and with the mechanical balance that is adapted so as to take into account this particularity. As a principal ingredient, the kinematical choice is based on the *natural* multiplicative decomposition of the deformation gradient into its known part at a precedent time and the relative deformation gradient.

The early age creep has been motivated by the classical generalized Maxwell model. This latter has been adapted to the present kinematical choice. Among others, only two parameters are newly introduced in addition to the incremental equilibrium elasticity: a characteristic time, and an adimensional factor representing the amplitude of the over-stress with respect to the equilibrium incremental elasticity. A model example has been detailed where the equilibrium part is based on a neoHooke-type incremental elasticity.

The main particularities of the algorithmic treatment have been proposed for an easy implementation within the context of the finite element method. The effort is of the order of that devoted to incremental finite strain elastic computations. The additional over-stress contribution reduces to the resolution of the discrete local evolution equation at the level of the integration points, together with the corresponding contribution to the algorithmic tangent moduli. The numerical examples have shown the efficiency of the whole numerical procedure. In particular, eventual structural buckling can be captured. This feature could certainly help the optimization of the printing process through simulations that could limit the number of costly physical experiments. More complex structures will be considered in the near future.

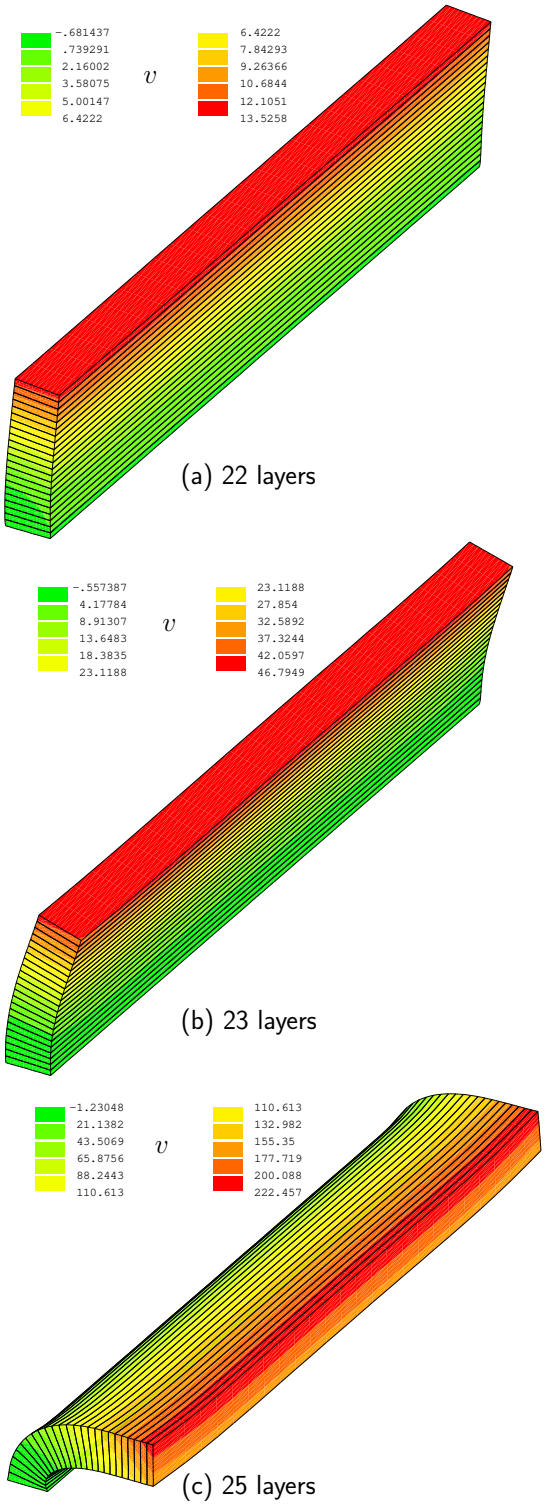

Fig. 10 Case 2 with $f = 1$ and $\tau = 10\,\text{min}$: deformed configurations and displacement field v for the 1 m wall after: (a) 22 layers, (b) 23 layers and, (c) 25 layers. Here the printing speed is 0.3 min per layer.

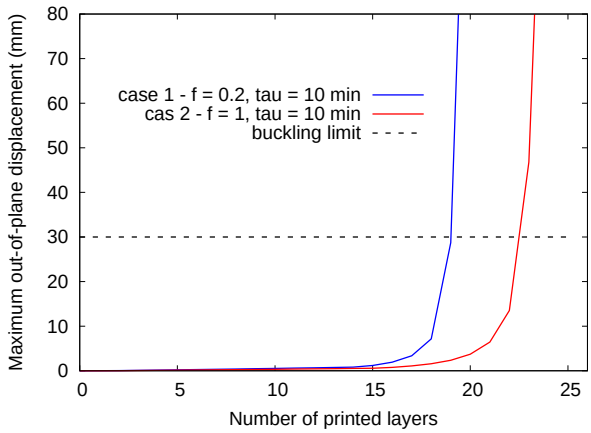

Fig. 11 Comparative evolution of the maximum out-of-plane displacement versus the number of the printed layers for the two simulations of the 1 m straight wall.

We believe that the modelling framework developped in this paper can trigger deeper research. For instance, a future step can be the coupling with the hydration of concrete that, in turn, is strongly coupled to the exothermy of the hydration reaction, i.e. through the Arrhenius law. And last but not least, it goes without saying that the present framework can easily be applied to the manufacturing of classical 3D printed polymers.

References

1. Bažant, Z.P., ed.: Mathematical modeling of creep and shrinkage of concrete. Wiley, New York (1988)
2. Benboudjema, F., Torrenti, J.M.: Early-age behaviour of concrete nuclear containments. Nuclear Engineering and Design **238(10)**, 2495–2506 (2008)
3. Craveiro, F., Duarte, J.P., Bartolo, H., Bartolo, P.J.: Additive manufacturing as an enabling technology for digital construction: A perspective on construction 4.0. Automation in Construction **103**, 251–267 (2019)
4. De Schutter, G., Taerwe, L.: Degree of hydration based description of mechanical properties of early-age concrete. Materials and Structures **29**, 335–344 (1996)
5. Hauggaard, A.B., Damkilde, L., Hansen, P.F.: Transitional thermal creep of early age concrete. Journal of Engineering Mechanics **125**, 458–465 (1999)
6. Holzapfel, G.A.: Nonlinear Solid Mechanics. A Continuum Approach for Engineering. John Wiley and Sons, Ltd, Chichester, West Sussex, UK (2000)
7. Kaliske, M., Rothert, H.: Formulation and implementation of three-dimensional viscoelasticity at small and finite strains. Computational Mechanics **19**, 228–239 (1997)
8. Kruger, J., Zeranka, S., van Zijl, G.: 3D concrete printing: A lower bound analytical model for buildability performance quantification. Automation in Construction **106**, 102904 (2019)
9. Labonnote, N., Ronnquist, A., Manum, B., Rüther, P.: Additive construction: state-of-the-art, challenges and opportunities. Automation in Construction **72(3)**, 347–366 (2016)
10. Lim, S., Buswell, R.A., Le, T.T., Austin, S.A., Gibb, A.F.G., Thorpe, T.: Developments in construction-scale additive manufacturing processes. Automation in Construction **21**, 262–268 (2012)
11. Marsden, J.E., Hughes, T.J.R.: Mathematical foundations of elasticity. Prentice-Hall, Englewood-Cliffs, New Jersey (1983)
12. Nair, S.A.O., Alghamdi, H., Arora, A., Mehdipour, I., Sant, G., Neithalath, N.: Linking fresh paste microstructure, rheology and extrusion characteristics of cementitious binders for 3D printing. Journal of the American Ceramic Society **102**, 3951–3964 (2019)
13. Nedjar, B.: On constitutive models of finite elasticity with possible zero apparent Poisson's ratio. International Journal of Solids and Structures **91**, 72–77 (2016)
14. Nedjar, B.: On a geometrically nonlinear incremental formulation for the modeling of 3D concrete printing. Mechanics Research Communications **116**, 103748 (2021). DOI https://doi.org/10.1016/j.mechrescom.2021.103748
15. Nedjar, B., Baaser, H., Martin, R.J., Neff, P.: A finite element implementation of the isotropic exponentiated Hencky-logarithmic model and simulation of the eversion of elastic tubes. Computational Mechanics **62(4)**, 635–654 (2018)
16. Ogden, R.W.: Non-linear Elastic Deformations. Dover, New York (1997)
17. Panda, B., Lim, J.H., Tan, M.J.: Mechanical properties and deformation behaviour of early age concrete in the context of digital construction. Composites Part B **165**, 563–571 (2019)
18. Simo, J.C.: Numerical analysis and simulation of plasticity. In: P. Ciarlet, J. Lions (eds.) Handbook of Numerical Analysis, vol. VI, pp. 183–499. North-Holland (1998)
19. Simo, J.C., Hughes, T.J.R.: Computational Inelasticity. Springer-Verlag, New York (1998)
20. Suiker, A.S.J.: Mechanical performance of wall structures in 3D printing processes: Theory, design tools and experiments. International Journal of Mechanical Sciences **137**, 145–170 (2018)
21. Wolfs, R.J.M., Bos, F.P., Salet, T.A.M.: Early age mechanical behaviour of 3D printed concrete: Numerical modelling and experimental testing. Cement and Concrete Research **106**, 103–116 (2018)
22. Wolfs, R.J.M., Bos, F.P., Salet, T.A.M.: Triaxial comression testing on early age concrete for numerical analysis of 3D concrete printing. Cement and Concrete Composites **104**, 103344 (2019)
23. Wolfs, R.J.M., Suiker, A.S.J.: Structural failure during extrusion-based 3D printinf processes. The International Journal of Advanced Manufacturing Technology **104**, 565–584 (2019)
24. Wriggers, P.: Nonlinear Finite Element Methods. Springer-Verlag, Berlin, Heidelberg (2008)
25. Zhang, J., Wang, J., Dong, S., Han, B.: A review of the current progress and application of 3D printed concrete. Composites Part A **125**, 105533 (2019)
26. Zohdi, T.I.: Modeling and Simulation of Functionalized Materials for Additive Manufacturing and 3D Printing: Continuous and Discrete Media: Continuum and Discrete Element Methods, vol. 60. Springer (2017)